Temporal Variability of the Overturning Circulation in the Arctic Ocean and the Associated Heat and Freshwater Transports during 2004–10

TAKAMASA TSUBOUCHI,[a] WILKEN-JON VON APPEN,[a] TORSTEN KANZOW,[a] AND LAURA DE STEUR[b]

[a] *Alfred Wegener Institute for Polar and Marine Research, Bremerhaven, Germany*
[b] *Norwegian Polar Institute, Tromsø, Norway*

(Manuscript received 31 March 2023, in final form 25 July 2023, accepted 27 July 2023)

ABSTRACT: This study quantifies the overturning circulation in the Arctic Ocean and associated heat transport (HT) and freshwater transport (FWT) from October 2004 to May 2010 based on hydrographic and current observations. Our main data source consists of 1165 moored instrument records in the four Arctic main gateways: Davis Strait, Fram Strait, Bering Strait, and the Barents Sea Opening. We employ a box inverse model to obtain mass and salt balanced velocity fields, which are then used to quantify the overturning circulation as well as HT and FWT. Atlantic Water is transformed into two different water masses in the Arctic Ocean at a rate of 4.3 Sv (1 Sv $\equiv 10^6$ m^3 s^{-1}). Combined with 0.7 Sv of Bering Strait inflow and 0.15 Sv of surface freshwater flux, 2.2 Sv flows back to the south through Davis Strait and western Fram Strait as the upper limb of the overturning circulation, and 2.9 Sv returns southward through Fram Strait as the lower limb of the overturning. The Arctic Ocean imports heat of 180 ± 57 TW (long-term mean ± standard deviation of monthly means) with a methodological uncertainty of 20 TW and exports FW of 156 ± 91 mSv with an uncertainty of 61 mSv over the 6 years with a potential offset of ~30 mSv. The HT and FWT have large seasonalities ranging between 110 and 260 TW (maximum in winter) and between 40 and 260 mSv (maximum in winter), respectively. The obtained overturning circulation and associated HT and FWT presented here are vital information to better understand the northern extent of the Atlantic meridional overturning circulation.

KEYWORDS: Arctic; Mass fluxes/transport; Meridional overturning circulation; Ocean circulation; Inversions

1. Introduction

The Arctic climate system has been changing rapidly over the last decades, as witnessed by a rapid rise in surface air temperature and a reduction in sea ice extent and thickness (Druckenmiller et al. 2022), melting of the Greenland ice sheet (The IMBIE Team 2020), the "Atlantification" of the Eurasian basin (Polyakov et al. 2017), and freshwater (FW) content accumulation in the Beaufort Gyre (Proshutinsky et al. 2019). Because of the Arctic amplification, the Arctic is the region on the globe where the largest increase in surface air temperature is expected to occur by the end of the century (IPCC 2021). All of these ongoing changes manifest themselves in changes in the Arctic climate system components such as atmosphere, ocean, and cryosphere. Ultimately, these changes are driven by the exchange of heat and FW across the lateral boundary of the Arctic atmosphere and ocean due to large-scale atmospheric circulation and ocean circulation (von Schuckmann et al. 2020). Among the CMIP5 global climate models, it is not clear whether atmospheric circulation or oceanic circulation will be the primary driver of continued future Arctic warming (Burgard and Notz 2017).

In the North Atlantic Ocean, the basinwide Atlantic meridional overturning circulation (AMOC) brings heat to the north well into the Arctic, and exports FW and dense water from the Arctic to the south (Dickson et al. 2008). The North Atlantic Current, which originates from the Gulf Stream, flows northward, and the portion of the Atlantic Water (AW) that crosses the Greenland–Scotland Ridge and enters the Norwegian Sea experiences substantial cooling and densification. A portion of it flows into the Arctic Ocean via the Barents Sea Opening (BSO) and Fram Strait and experiences further water-mass transformations. The other part recirculates in Fram Strait, partially subducts beneath surface water and returns south along the East Greenland Current (EGC) in the Nordic seas (Mauritzen 1996). In addition, about one-third of the dense water is formed in the Iceland Sea (Våge et al. 2011), which, merged with the dense water in the EGC, flows toward the Greenland–Scotland Ridge as headwaters of the overflow water, eventually feeding the lower limb of the AMOC (Hansen and Østerhus 2000). It has been shown that about half of the Polar Water exiting the Arctic participates in the overturning circulation (Le Bras et al. 2021) but how much water-mass transformation occurs in the Arctic Ocean and how that may change in the future is still unclear.

There are a few sustained basinwide scale mooring arrays in the North Atlantic to monitor the temporal variability of AMOC and the associated heat transport (HT) and FW transport (FWT; Frajka-Williams et al. 2019). Going from south to north, they include the "RAPID" array across the subtropical gyre since 2004 (Cunningham et al. 2007), the Overturning in

Denotes content that is immediately available upon publication as open access.

Supplemental information related to this paper is available at the Journals Online website: https://doi.org/10.1175/JPO-D-23-0056.s1.

Corresponding author: Takamasa Tsubouchi, t.tsubouchi@met.kishou.go.jp

DOI: 10.1175/JPO-D-23-0056.1

the Subpolar North Atlantic Program (OSNAP) array across the subpolar gyre since 2014 (Lozier et al. 2019), the Greenland–Scotland Ridge array since 1992 (Østerhus et al. 2019), and the Arctic boundary array since 2004 (Dickson et al. 2008). To quantify the HT and FWT, one needs to measure all inflow and outflow branches at the same time. The HT can then be quantified as the temperature difference between the inflow and outflow and is proportional to the strength of the ocean circulation (Hall and Bryden 1982; Ganachaud and Wunsch 2000). In a similar manner, FWT can be quantified as the salinity difference between the inflow and outflow scaled by the ocean circulation (Ganachaud and Wunsch 2003).

Although there are many numerical models available at increasingly better resolutions, there are still significant discrepancies relative to the observations and among models. This not only holds for climate models that deliver future climate projections (Wang et al. 2016; Ilıcak et al. 2016) but also for data assimilation models to assess the state of the ocean in the present and past (Uotila et al. 2018; Mayer et al. 2019). Moreover, the Arctic Ocean lacks sufficient observation-based datasets to validate these numerical ocean and climate models. For the net Arctic Ocean transports, there are only a few datasets available that cover the entire Arctic Ocean. Considering the ongoing fast changes in the Arctic climate, there is an urgent need to establish and update the observation-based Arctic Ocean transport estimates.

The Arctic Ocean is delineated from the rest of the ocean by (from east to west) Fram Strait between Greenland and Svalbard, BSO between Svalbard and Norway, Bering Strait between Siberia and Alaska, Fury and Hecla Strait between the Canadian mainland and Baffin Island, and Davis Strait between Baffin Island and Greenland, of which Fury and Hecla Strait can be ignored to estimate the water-mass exchanges between the Arctic Ocean and the surrounding seas (Tsubouchi et al. 2012; Bacon et al. 2022). To quantify the Arctic Ocean transports, synoptic hydrographic data from these four Arctic gateways were analyzed using a box inverse model (Tsubouchi et al. 2012). This inverse box model was then applied to the mooring data from the Arctic gateways to obtain a 1-yr-long estimate between September 2005 and August 2006 (Tsubouchi et al. 2018, hereafter T2018). This study employs the same inverse method to extend the time series from 1 year (T2018) to 6 years (2004–10) to quantify representative seasonal cycles and investigate interannual variability. We also exploit the mass and salt conserved velocity field to estimate the overturning circulation in the Arctic Ocean and its temporal variability.

2. Data and methods

In this section, we first present the datasets used in this study. We then describe the method to generate gridded monthly-mean properties and velocity fields. Third, we show the inverse model method and then HT and FWT calculations.

a. Data

Our main oceanographic measurements consist of 1165 moored instrument records in Davis, Fram, and Bering Straits and the BSO (Fig. 1). The moored instruments comprise devices measuring point measurements of temperature, salinity and pressure; acoustic Doppler current profilers (ADCPs); and single-point current meters. Their typical deployment duration is 1 or 2 years, with sampling rates of 10–60 min. The mooring array configuration from summer 2005 to summer 2006 was presented in Fig. 1 of T2018, and a similar configuration was maintained from summer 2004 to summer 2010. Due to various reasons, the number of observational records of good quality at each mooring site varied from year to year (Fig. S1 in the online supplemental material). Details of the in situ mooring data in terms of measurement locations and durations, type of instruments, measurement accuracy, original sampling rate, and so on, can be found as follows: Davis Strait in Curry et al. (2014); the western side of Fram Strait in de Steur et al. (2014) with the data at de Steur (2019); the central and eastern side of Fram Strait in Beszczynska-Möller et al. (2012) with the data at Beszczynska-Möller et al. (2015); BSO in Ingvaldsen et al. (2004); and Bering Strait in Woodgate (2018).

In addition, for the BSO, 37 repeat CTD sections between Bear Island and Tromsø in Norway (i.e., around 6 occupations per year) are also included to compensate for the relatively small number of moored instrument records in BSO. Each CTD section comprises around 20 stations in ~30-km horizontal distance and has 1-dbar resolution in vertical coverage.

Sea ice thickness, sea ice temperature, and velocity data are obtained from the Pan-Arctic Ice Ocean Modeling and Assimilation System (PIOMAS; Zhang and Rothrock 2003). We choose to use this data assimilation product to obtain continuous sea ice transport estimates without data gaps. Model biases are evaluated as 8% in sea ice velocity and 9% in ice thickness with available buoy and submarine observations (Zhang and Rothrock 2003), and model ice thickness biases depend on ice thickness itself (model overestimate ice thickness of thinner than ~2 m; Johnson et al. 2012). These monthly data are used to quantify the sea ice volume transport, HT, and FWT through the four Arctic gateways.

b. Construction of monthly gridded fields

Based on the point measurements of temperature, salinity, and velocity at moored instrument locations, initial coast-to-coast and surface-to-bottom temperature, salinity, and cross-sectional velocity fields are obtained at monthly resolution. We focus on the period from October 2004 to May 2010 when most of the moored instrument records overlapped; several, but not all, arrays started earlier and/or have been continued thereafter. As in T2018, grid resolution is 3 km in the horizontal axis, and it has 75 vertical layers. There are, however, two major differences between this study and T2018: the treatment of missing data periods and unobserved variability outside of the mooring arrays. Details of the mooring data treatment, the gridding procedure, and major features of the gridded fields can be found in section a of the online supplemental material.

c. Box inverse model

The box inverse model employed in this study is the same as in T2018. It contains a set of linear equations that represent

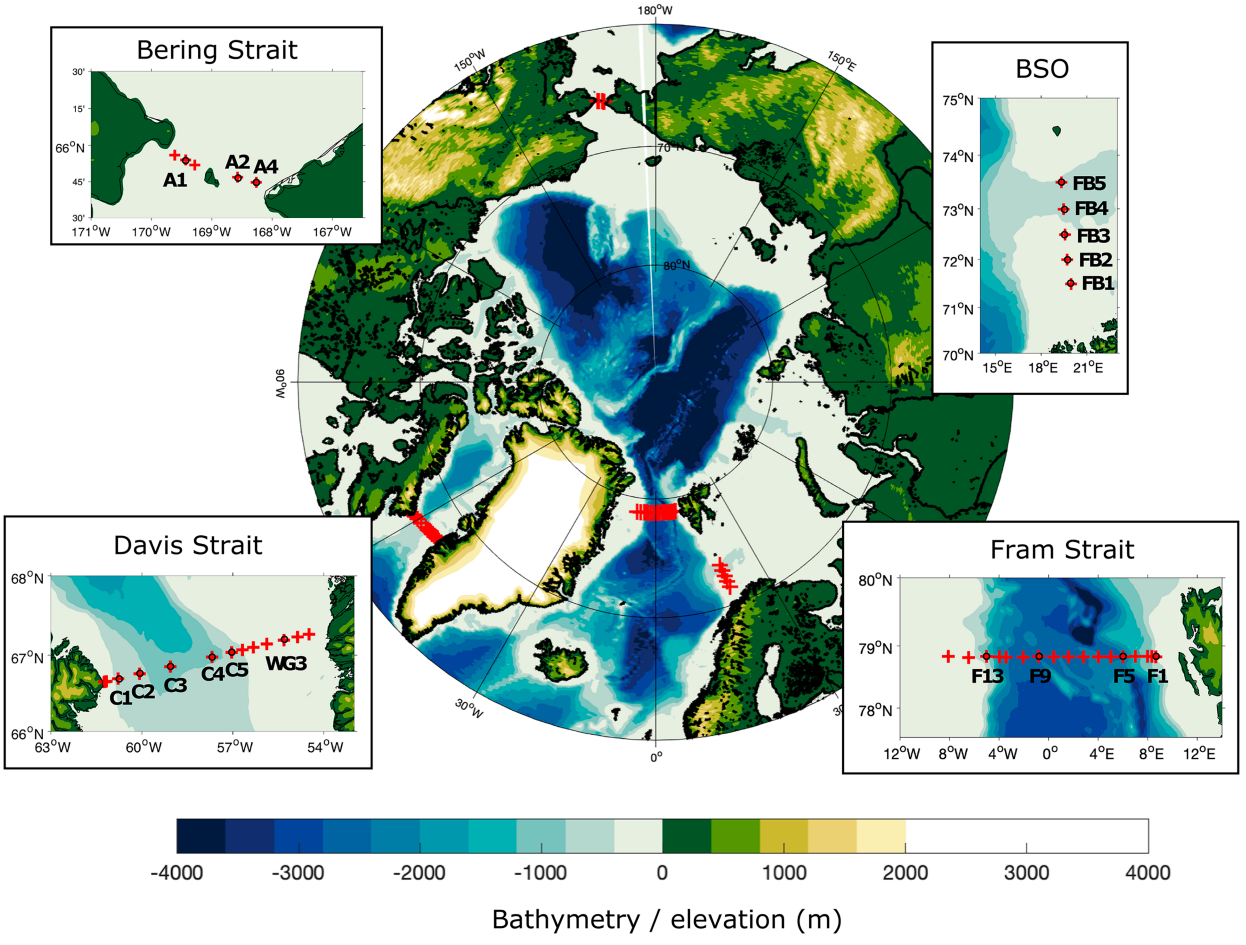

FIG. 1. Bathymetry of the Arctic Ocean and the configuration of mooring arrays in the Davis, Fram, and Bering Straits and the Barents Sea Opening (BSO). The locations of the mooring sites are shown with red crosses. Selected mooring sites are labeled and marked with black circles in each inserted panel.

mass and salt conservation for each defined model layer. Each equation considers four different types of physical mechanisms that exchange mass and salt. They are horizontal ocean circulation and sea ice export across the Arctic boundary (i.e., the four gateways), and surface FW flux through the sea surface of the Arctic Ocean, and diapycnal fluxes between model layers. The surface FW flux represents all FW that goes into the Arctic Ocean through the sea surface bounded by the four gateways. It is a sum of precipitation − evaporation ($P - E$) and river discharge from Eurasia, North America, the Canadian Arctic Archipelago, and Greenland. Since the accuracy of these transport estimates are different, the box inverse model objectively modifies these transport estimates according to the size of these uncertainties to achieve mass and salt conservation in each defined model layer.

We use the mooring data across the four Arctic gateways to estimate the first guess of horizontal ocean circulation, and PIOMAS data to estimate the first guess of horizontal sea ice export. Smaller uncertainties are assigned on these two terms (3-month standard deviation of moored velocity measurements and 10% magnitude of initial sea ice velocities, respectively). In contrast, we use no data for diapycnal fluxes and surface FW fluxes. Hence, constant values of zero diapycnal fluxes and 180-mSv surface FW flux are set as a first guess over the entire period, and larger uncertainties are assigned on these two terms [1×10^{-5} m^{-1} s^{-1} in diapycnal velocities, which are equivalent to ~10 Sv (1 Sv $\equiv 10^6$ m^3 s^{-1}) in diapycnal fluxes depending on area of model layer interfaces and 100% magnitude of the surface FW flux initial estimate]. For each month, diapycnal fluxes across model layer interfaces and surface FW fluxes are obtained as results from the inverse solutions.

We define five model layers (Table 1): Surface Water (SURF) layer, Upper Atlantic Water (UAW) layer, Atlantic Water (AW) layer, Intermediate Water (IW) layer, and Deep Water (DW) layer. The water-mass definitions are the same as in T2018, with one change in model layer interface definitions. The model layer interface between AW and IW is now defined by the 2°C isothermal and that between IW and DW is defined by a fixed depth of 1500 m instead of isopycnal definitions. This change is motivated by the fact that there are only three point measurements of salinity in Fram Strait below 750 m during this period. The 2°C isotherm in the eastern

TABLE 1. Definitions of the five model layers and corresponding water masses.

Model layer	Layer name	Layer abbreviation	Upper interface	Lower interface
1	Surface water	SURF	Surface	27.10 kg m^{-3}
2	Upper Atlantic water	UAW	27.10 kg m^{-3}	27.50 kg m^{-3}
3	Atlantic water	AW	27.50 kg m^{-3}	2.0°C[a]
4	Intermediate water	IW	2.0°C	1500 m
5	Deep water	DW	1500 m	Bottom
6	Full depth		Surface	Bottom

[a] The 2°C isotherm in the eastern and central Fram Strait mostly coincides with the depth of 27.97 kg m^{-3} isopycnal, which defines the AW lower boundary (Beszczynska-Möller et al. 2012).

and central Fram Strait mostly coincides with potential density isopycnal of 27.97 kg m^{-3}, which defines the AW lower boundary (Beszczynska-Möller et al. 2012). These choices avoid defining unrealistic shapes of layer interfaces between AW and IW and between IW and DW due to the sparse salinity measurements.

The inverse model has 12 constraints that come from volume and salt transport constraints for the full depth and the 5 defined layers and 1287 unknowns that represent the four different types of physical mechanisms that exchange mass and salt. The 1287 unknowns are categorized into bottom velocities at 3 km grid points (639 unknowns), sea ice advections at these grid points (639 unknowns), surface FW flux (1 unknown), and diapycnal velocities across defined water-mass interfaces (8 unknowns). Row and column weights are set to prescribe uncertainties both on constraints and unknowns. The row- and column-weighted matrix was then solved by the singular value decomposition (SVD). A posteriori uncertainties were calculated based on the Gauss–Markov formalism (Wunsch 1996). Details of the box inverse model setting are provided in appendix A in T2018.

The box inverse model solutions in this study are similar to that in T2018. The eight leading SVD modes are used to solve the 12 conservation equations that yield a stable solution in which the inverse model solution for the unknowns remains within a priori uncertainties. Overall, reference velocities are modified by mean and peak perturbations of 2 and 10 mm s^{-1}, respectively. Larger modification is introduced over Belgica Bank in Fram Strait and north of Bear Island in BSO where moored observations do not exist. As discussed in the online supplemental material (see Fig. S3), most of the full-depth initial imbalances stem from below 1500 m in Fram Strait. Thus, most of the inverse adjustment occurs in Fram Strait and accounts for 2.8 ± 1.7 Sv [mean ± standard deviation (std)]. Adjustments in other gateways are minor: BSO for 0.1 ± 0.4 Sv, Davis Strait for 0.0 ± 0.1 Sv, and Bering Strait for 0.0 ± 0.0 Sv (mean ± std). Sea ice transport adjustments are also minor, equivalent to 0.5 mSv on average with a peak of 3 mSv. The surface FW flux adjustment and the diagnosed diapycnal flux adjustments are larger. The former is equivalent to 20 mSv with a peak of 300 mSv. The latter is equivalent to 1–3 Sv on average with a peak of 6 Sv.

d. HT and FWT calculation

HT through the Arctic boundary is calculated as (following T2018)

$$\mathrm{HT} = \int\int \left[\rho_o c_p^o (v'\theta')^o + \rho_i c_p^i (v'\theta')^i + \rho_i c_f (v)^i\right] dx\, dz, \quad (1)$$

where ρ_o is density of seawater (1027 kg m^{-3}), c_p^o is specific heat capacity of seawater (3.987×10^3 J kg^{-1} K^{-1}), v' is the cross-sectional velocity anomaly from the mean $\overline{v}$, and θ' is the potential temperature difference from its reference value $\overline{\theta}$. Note that $\overline{v}$ is not zero. It is a small number [$O(10^{-4})$ m s^{-1}] that balances with the surface FW flux in the mass conservation. Superscripts o and i refer to liquid ocean and sea ice, respectively. The ρ_i is density of sea ice (930 kg m^{-3}), c_p^i is specific heat capacity of sea ice, c_f is latent heat of freezing (3.347×10^5 J kg^{-1}), v is the cross-sectional velocity, z is depth, and x is the along-boundary coordinate. Similarly, FWT through the Arctic boundary is calculated as

$$\mathrm{FWT} = \frac{1}{\overline{S}} \int\int \left[(v'S')^o + (v'S')^i\right] dx\, dz, \quad (2)$$

where S' is the salinity difference from its reference value $\overline{S}$. The reference values $\overline{\theta}$ and $\overline{S}$ are calculated for each individual month as the appropriate boundary-mean potential temperature and salinity, respectively (Bacon et al. 2015). To estimate the FWT related to sea ice, a sea ice salinity of 6 is assumed, which represents the salinity of first year sea ice (Kovacs 1996).

3. Results

a. Mass and salt balanced velocity fields and gateway volume transports

Figures 2a–c show the 68-month mean mass and salt balanced absolute velocity field, along with cumulative full depth and water-mass specific volume transports. Positive values indicate inflow into the Arctic Ocean. Table 2 summarizes volume transport estimates through the four gateways and the overturning cells (the latter will be discussed in the next section). The mean absolute velocity field captures major features of ocean circulation around the Arctic boundary. The major export of water happens on both sides of Greenland. In the western Davis Strait water is exported as the SURF water mass (1.8 Sv). In the western Fram Strait, export of SURF is small (0.7 Sv) and the EGC primarily exports IW (4.0 Sv) and DW (1.5 Sv). AW is transported into the Arctic Ocean by the WSC (3.5 Sv) through the eastern Fram Strait and through the BSO (1.1 Sv). BSO also imports 1.1 Sv of the SURF and

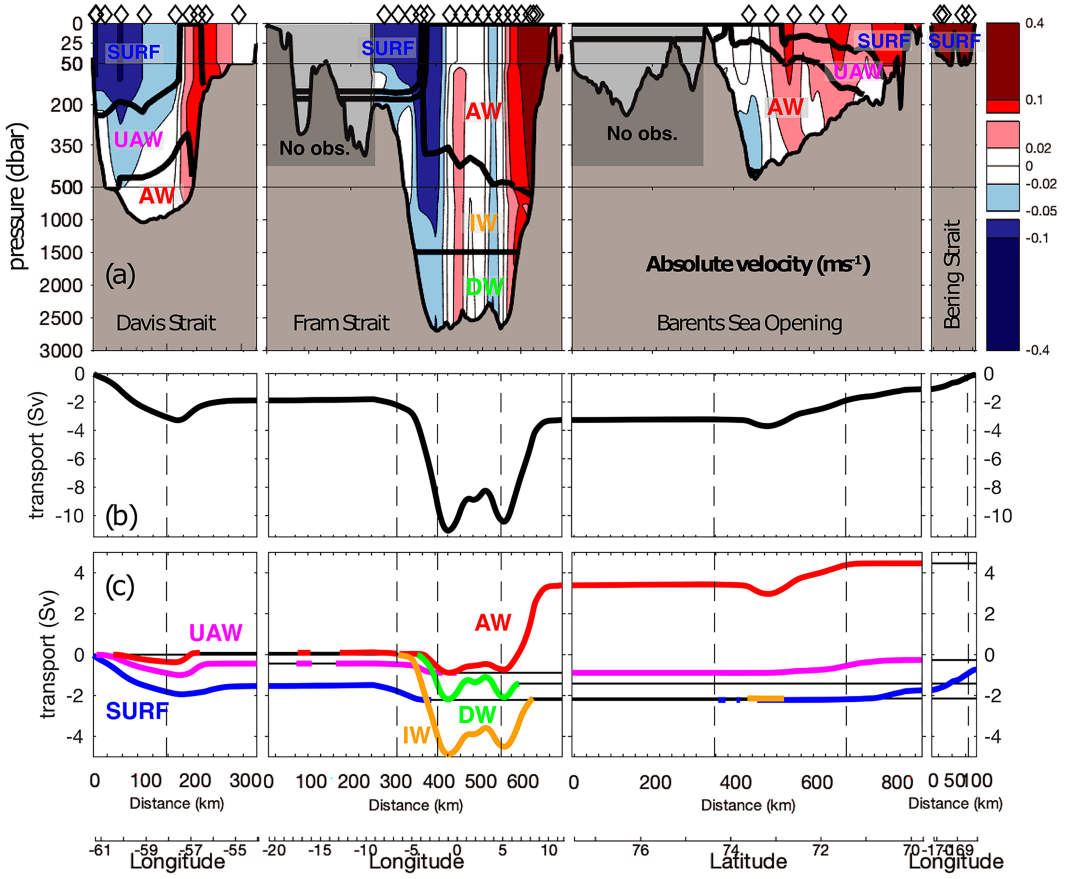

FIG. 2. (a) The 68-month mean mass and salt balanced absolute velocity field (m s^{-1}) around the Arctic boundary. Thick black lines show defined water-mass boundaries. Red and blue colors respectively show inflow to and outflow from the Arctic Ocean. Diamonds show mooring-site locations. (b) The 68-month mean full-depth volume transport (Sv) accumulated around the boundary. (c) Accumulated volume transport (Sv) for each water mass in different colors: SURF in blue, UAW in magenta, AW in red, IW in orange, and DW in green. Where a specific water mass is absent from the section, the accumulated transport is plotted as a black line.

UAW layers combined. Bering Strait imports 1.0 Sv Pacific water in the SURF layer.

Figure 3 shows volume transport time series for the four gateways and their mean seasonal cycles. The long-term mean and their seasonality generally agree with previous estimates [Davis Strait for Curry et al. (2014); the western Fram Strait for de Steur et al. (2014); the central and eastern Fram Strait for Beszczynska-Möller et al. (2012); BSO for Ingvaldsen et al. (2004); Bering Strait for Woodgate (2018)]. What is new here is that the obtained volume transport time series satisfies mass and salt conservation at any given month. The net volume transport (black line in Fig. 3) is small and balances with sea ice export through the four gateways and the surface FW flux. We find that the transport in each gateway is subject to substantial interannual variability and has a clear seasonality as summarized in Table 2, which was not obvious from 1-yr data presented in T2018. BSO inflow is the strongest in winter at 2.9 Sv [January–March (JFM) mean], and the weakest in spring at 1.3 Sv [April–June (AMJ) mean]. In contrast, Bering Strait inflow is the strongest in summer at 1.4 Sv [July–September (JAS) mean] and the weakest in autumn at 0.7 Sv [October–December (OND) mean] in agreement with Woodgate (2018). Seasonality in Davis Strait and Fram Strait are the outcome of two-way compensating current systems within each strait. In Davis Strait, weaker net volume transport in September–December coincides with a stronger cyclonic circulation along the section: stronger southward Arctic origin water in the west and stronger northward water in the east (Curry et al. 2014). In Fram Strait, stronger net volume transport from October to March coincides with an enhanced cyclonic circulation in winter due to a stronger EGC (de Steur et al. 2014) and a stronger WSC (von Appen et al. 2016). We estimate −9.0 Sv for the EGC and 9.2 Sv for the WSC in winter (JFM mean) and −5.3 Sv for the EGC and 4.6 Sv for the WSC in summer (JAS mean).

b. *Overturning circulation in the Arctic Ocean*

The transport obtained across the Arctic Ocean boundary is converted into temperature–salinity space and illustrates the water-mass transformation that occurs in the Arctic Ocean

TABLE 2. Mean and standard deviation (std) of ocean volume transports (Sv) in the four Arctic main gateways and of the three overturning cells between October 2004 and May 2010 (column 2) and their seasonal averages (columns 3–6). Sign conventions for the four main gateways are positive means inflow to the Arctic Ocean and negative means outflow from the Arctic Ocean. For the overturning cells, positive means that inflow density is lighter than outflow density, and vice versa. Note that we consider Polar Water as the sum of SURF + UAW.

		Seasonal averages			
	Mean ± std (Sv)	JFM	AMJ	JAS	OND
Four main gateways					
Davis Strait	−1.9 ± 1.0	−1.8	−2.2	−2.4	−1.2
Fram Strait	−1.4 ± 1.2	−2.0	−0.4	−1.2	−1.9
BSO	2.2 ± 1.0	2.9	1.3	2.2	2.4
Bering Strait	1.0 ± 0.5	0.8	1.3	1.4	0.7
Overturning cells					
Pacific Water to Polar Water (SURF + UAW)	0.7 ± 0.6	0.1	0.7	1.2	0.4
AW to Polar Water	−1.4 ± 0.8	−1.9	−1.3	−0.4	−1.1
AW to both IW and DW	2.9 ± 1.2	3.1	1.8	2.5	3.7

(Fig. 4a). Most of the inflow takes place in the AW inflow between 2.0° and 7.5°C in potential temperature and 34.8 to 35.2 in salinity shown by the red colors. This AW inflow is transformed into the salty-cold deeper outflow (potential density greater than 27.8 kg m^{-3}) and into fresher upper outflowing Polar Water (which we define as the sum of SURF and UAW, i.e., with potential density less than 27.5 kg m^{-3}). The volume transport as a function of potential density provides the overturning streamfunction in the Arctic Ocean (black line in Fig. 4b). Contributions to the mean overturning circulation in the Arctic Ocean from the four Arctic gateways are shown individually in different colors. The mean overturning streamfunction crosses zero transport twice, at about 26.6 and 27.7 kg m^{-3}, indicating that there are three overturning cells. The upper cell appears in density less than 26.6 kg m^{-3} with a maximum of 0.3 Sv around 26.3 kg m^{-3}. This cell transforms the Pacific water inflow through Bering Strait into the Polar Water outflow through both Davis Strait and Fram Strait, with the outflow being denser than the inflow. Since this water comes from the Pacific Ocean and exits to the North Atlantic via the Labrador Sea and Nordic seas, it does not constitute an overturning cell in the classical sense (i.e., water returning to the basin from where it came from, after the density transformation occurred). The intermediate cell has a strength of −1.1 Sv around 27.5 kg m^{-3}, which is the interface between UAW and AW. The negative value of the strength of the cell implies that this cell represents the transformation of the (relatively) denser AW inflow through the BSO and Fram Strait into the (relatively) lighter Polar Water outflow through Davis Strait and Fram Strait. The transformation is accomplished within the Arctic Ocean by mixing of AW with sea ice meltwater and river freshwater runoff and precipitation. The lowest cell has a maximum of 2.7 Sv around 28.0 kg m^{-3}, that is, the interface between AW and IW. This cell transforms AW inflow through Fram Strait and BSO into denser waters (IW and DW), which exit the Arctic Ocean through Fram Strait.

The monthly time series of the strength of the three cells and their corresponding seasonal cycles are shown in Figs. 4c and 4d, respectively. Throughout the observational period the upper cell (blue line) shows the smallest variability, whereas the lower cell (green line) shows the largest. While the upper cell mostly displays (intra)seasonal variability, the intermediate and deep ones also feature interannual changes. Occasionally, the strengths of both the upper and intermediate cells drop to 0 Sv. We next examine the seasonal cycle of the overturning circulation. The intermediate overturning cell (AW to SURF/UAW conversion in red line) is strongest in winter (February–March) and weakest in summer (August). The lower cell (AW

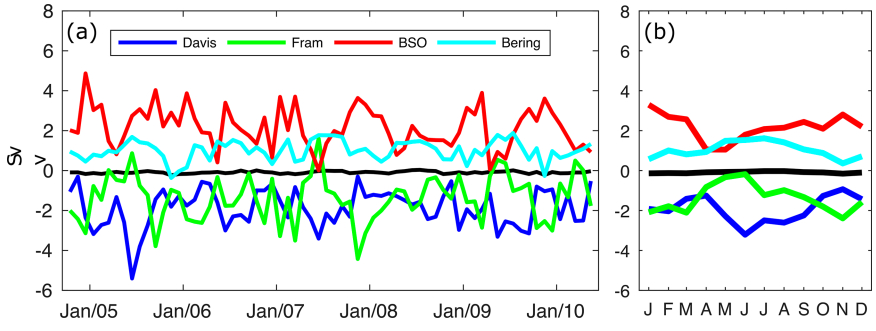

FIG. 3. (a) Ocean volume transport time series (Sv) in the four Arctic main gateways from October 2004 to May 2010: Davis Strait in blue, Fram Strait in green, BSO in red, and Bering Strait in cyan. The sum of these is shown in black. (b) Their mean seasonal cycles.

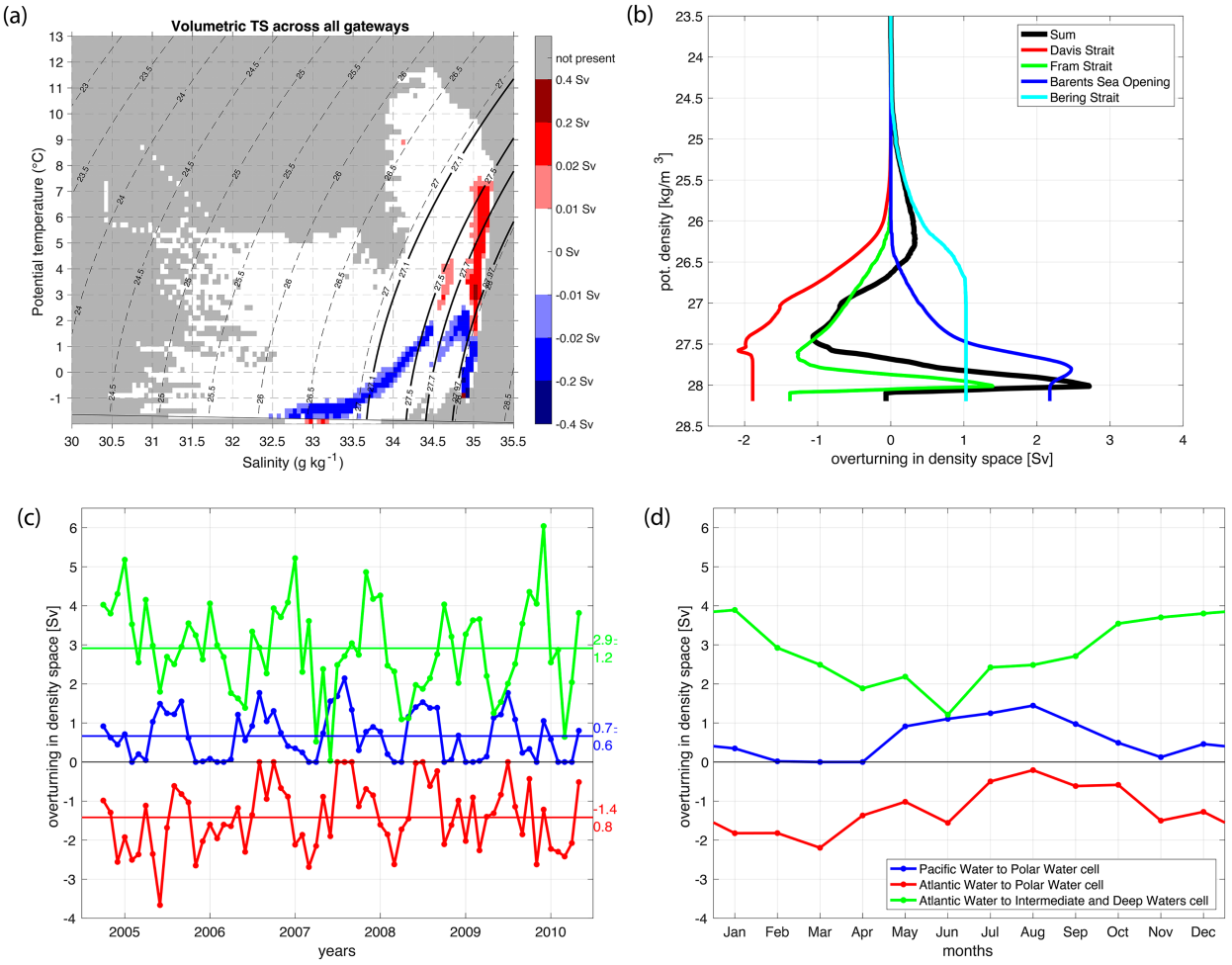

FIG. 4. (a) Volumetric temperature–salinity plot (monthly values) integrated across the Arctic boundary in $\Delta S = 0.05$ and $\Delta T = 0.2$°C boxes. Positive (red) values represent inflow, θ–S boxes with less than ±0.01 Sv are shown in white, and θ–S boxes with no contribution are shown in gray. (b) The mean overturning streamfunction calculated as a function of potential density (black line). Contributions from the individual gateways are shown in different colors. (c) Monthly time series of the three overturning cells: Pacific water to Polar Water cell in blue, AW to Polar Water cell in red, and AW to both IW and DW cell in green. Positive means that inflow density is lighter than outflow density, and vice versa. (d) Mean seasonal cycle of the three overturning cells.

to IW/DW conversion in green line) follows a similar pattern but reaches its extreme values slightly earlier (maximum in January; minimum in June). While it can be expected that IW formation is maximum in wintertime during the massive cooling of both the BSO inflow over the shallow Barents Sea and of the Fram Strait branch of Atlantic Water inflow, this does not necessarily lead to a maximum IW outflow during winter in Fram Strait, as water masses formed in the Arctic Ocean can take many years before being exported. Rather, we expect the seasonality observed in the two AW-related overturning cells to be primarily wind driven: Fig. 3b demonstrates the BSO inflow peak occurring in January, which is mostly wind driven, to coincide with the timing of maximum AW–IW/DW overturning. The summertime maximum of the upper overturning cell in Fig. 4d coincides with the maximum in low-density inflow through Bering Strait and the maximum outflow through Davis Strait at that time of the year in Fig. 3b.

Table 2 summarizes the overturning circulation in the Arctic Ocean. A total of 2.2 Sv Polar Water outflow is fed by three sources: 0.7 Sv Pacific water inflow, 0.15 Sv surface FW flux, and 1.4 Sv AW. The lower limb of the overturning circulation of 2.9 Sv is fed by the AW inflow. Note that these transport numbers are the 68-month averages of the monthly time series of the three overturning cells in Fig. 4c, which is higher than the two maxima and the one minimum of the mean overturning function in Fig. 4b. See Fig. S4 in the online supplemental material for the details.

c. *HT and FWT time series*

Another main result of this study is the HT and FWT time series from October 2004 to May 2010 (Fig. 5). Table 3 summarizes the 68-month mean and annual mean values. Here, positive values of HT mean the Arctic Ocean gains heat from the surrounding seas. As the 6-yr mean, the Arctic Ocean

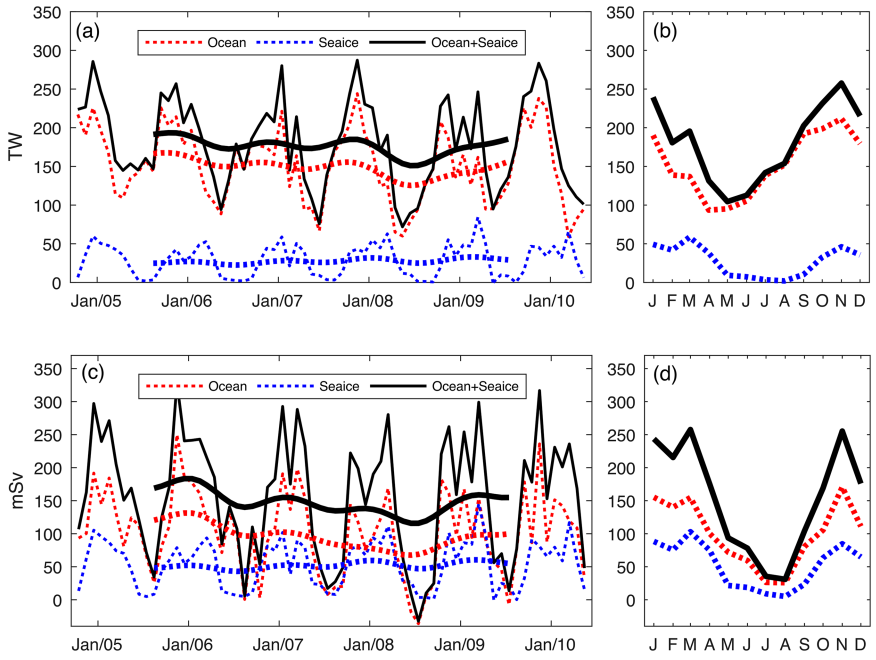

FIG. 5. (a) The boundary HT time series (TW) from October 2004 to May 2010: the ocean component is in dotted red lines, the sea ice component is in dotted blue lines, and the sum of them is in solid black lines. Thick lines show smoothed time series using a 21-point Hanning filter. (b) The mean HT seasonal cycles. (c) As in (a), but for FWT time series (mSv). (d) The mean FWT seasonal cycles.

imports 180 ± 57 TW (mean ± std) of heat, with an ocean contribution of 151 ± 48 TW and a sea ice contribution of 29 ± 21 TW. It has a large month to month variability ranging from ~80 to ~290 TW (Fig. 5b). It also shows a clear seasonality with a maximum in November around ~260 TW, and minimum in May around ~110 TW. The seasonality is primarily driven by ocean heat transport. In addition, there is substantial interannual variability. The largest annual mean HT of 195 TW was observed in 2009, while the lowest of 155 TW in 2008. This interannual variability seen here is dictated by the ocean heat transport and not that of sea ice.

TABLE 3. Mean and std of the Arctic boundary HT (TW) and FWT (mSv) between October 2004 and May 2010 (column 2). Total HT and FWT are the sum of ocean transport and sea ice transport. Their annual mean (January–December) values are also shown (columns 3–7). Positive HT means that the Arctic Ocean imports heat from the surrounding seas. Positive FWT means that the Arctic Ocean exports FW to the surrounding seas.

	Mean ± std	2005	2006	2007	2008	2009
HT (TW)						
Ocean	151 ± 48	166	150	158	127	162
Sea ice	29 ± 21	27	25	28	27	32
Total	180 ± 57	193	175	185	155	195
FWT (mSv)						
Ocean	102 ± 63	125	98	97	76	105
Sea ice	54 ± 36	53	47	52	51	60
Total	156 ± 91	177	145	150	127	165

Figure 5c shows the Arctic boundary FWT time series. Positive values of FWT indicate net export from the Arctic Ocean and negative indicate net import of FW to the Arctic. The 68-month mean FWT is 156 ± 91 mSv (mean ± std) with an ocean contribution of 102 ± 63 mSv and a sea ice contribution of 54 ± 36 mSv (Table 3). The month-to-month variability is large, ranging from −40 mSv (net import of FW) to +320 mSv (net export of FW). The seasonal variability has higher values of ~230 mSv in winter months (November–March) and minima as lower values ~40 mSv in summer months (July–August). Approximately two-thirds of the monthly and seasonal variabilities come from the ocean and the other one-third comes from the sea ice. FWT also shows large interannual variability: the largest annual mean FWT of 177 mSv occurred in 2005 and the lowest annual mean of 127 mSv in 2008. The ocean FW transport explains 87% of the total year to year FW transport variability.

We now compare our result with T2018 to estimate potential offsets in HT and FTW due to the unobserved variability by moored instruments. T2018 uses the same data and same inverse model method for one year (i.e., 2005/06), but has different treatment of missing data periods and of the unobserved variability. T2018 estimates the unobserved variability above the shallowest moored instruments in Davis Strait, Fram Strait and Bering Strait using the vertical gradients of temperature, salinity and velocity from NEMO model output, for example (see the online supplemental material of T2018 for full details). Thus, we anticipate our FWT estimate may underestimate the transport by neglecting these unobserved

variabilities in the upper water column. Our oceanic HT estimate during T2018's study period of September 2005 to August 2006 is 161 ± 45 TW (mean ± std), agreeing well with the T2018 estimate of 154 ± 44 TW. Our oceanic FWT estimate is 125 ± 64 mSv (mean ± std) over this 1-yr period, as compared with T2018's estimate of 155 ± 64 mSv. To identify the source of the 30-mSv difference, integrated FWT anomaly in comparison with T2018 is examined (T2018 minus this study; Fig. S5 in the online supplemental material). The western Davis Strait has a positive anomaly of 24 mSv (less FWT in this study). The Belgica Bank in Fram Strait has a negative anomaly of 10 mSv (more FWT in this study) with ~50-mSv FWT associated with the anticyclonic circulation over the Belgica Bank. The EGC and WSC regions in Fram Strait show little anomaly where entire F10 mooring data and most of F3 mooring data were missing during 2005/06 (Fig. S1 in the online supplemental material), thus impacts of different missing data treatment methods could appear. These features are mostly consistent with Fig. 10c in T2018, which examines the impact of unobserved variability alone, but the anomaly over the Belgica Bank in Fram Strait is notably different (~10-mSv anomaly in this study versus ~20-mSv anomaly in T2018). This comes from different missing data treatment, such as inclusion of F17 mooring data (Fig. S1), highlighting uncertainty associated with the data gaps and interpolation methods. To conclude, this study likely underestimates the FWT by ~30 mSv by omitting unobserved variability over the shallowest moored instruments in western Davis Strait. The Belgica Bank in Fram Strait is also still a major source of uncertainty and likely is responsible for significant offsets in FWT (Karpouzoglou et al. 2023), but we do not have the means to investigate these in detail here.

Uncertainty of the obtained ocean HT and FWT stem from two different sources: (i) accuracy and representativeness of the measurements in the property and velocity fields, and (ii) unobserved variability both in the velocity and property fields with the mooring array configuration. We consider the accuracy and representativeness uncertainty (i) in the velocity fields based on the a posteriori error estimate of the inverse model that is originally prescribed as an a priori error in the boundary velocity fields based on the standard deviation of velocities measured by the moored instruments over three months as in Tsubouchi et al. (2012). We quantify this uncertainty in heat transport to be ±26 TW and that in FW transport to be ±44 mSv for a single month. For the unobserved variability uncertainty (ii), we adopt the uncertainty estimates from T2018, which is ±7 TW for HT and ±52 mSv for FWT. T2018 estimates this unobserved variability in FWT stems from three sources and their uncertainties are ~30 mSv each. They are the upper water column in western part of Davis Strait, the Belgica Bank in western Fram Strait, and sparse deep salinity measurements in the EGC region in Fram Strait. By combining these two different uncertainty estimates in a root sum square sense, we obtain that the total uncertainty for heat is ±27 TW and that for FW is ±68 mSv for a single month. To estimate the uncertainty for the long-term mean transport, we assume the former uncertainty to be half random and half systematic while the latter uncertainty is systematic. Random uncertainty can be reduced by frequent sampling with factor of $n^{-1/2}$, where n is the number of degrees of freedom. By calculating the random uncertainty with $n = 68$ and combining that with the systematic uncertainties in a root sum square sense, we estimate the long-term mean uncertainty for HT and FWT as ±20 TW and ±61 mSv, respectively.

d. Water-mass transformation

To better understand the HT and FWT variability and its relation to surface fluxes and storage fluxes, we view them from a water-mass transformation perspective as described in T2018. Unlike examining each gateway contribution individually, this approach is not affected by the choice of reference values. The Arctic heat and FW budgets can be expressed as

$$F_H^{\mathrm{Surf}} = -\rho_o c_p^o(\Theta_{\mathrm{in}} - \Theta_{\mathrm{out}}^{oi})V_{\mathrm{in}} + F_H^{\mathrm{stor}} \quad \text{and} \tag{3}$$

$$F_{\mathrm{vol}}^{\mathrm{surf}} = \frac{1}{S_{\mathrm{out}}^{oi}}(S_{\mathrm{in}} - S_{\mathrm{out}}^{oi})V_{\mathrm{in}} + F_{\mathrm{FW}}^{\mathrm{stor}}, \tag{4}$$

where F_H^{Surf} and $F_{\mathrm{vol}}^{\mathrm{Surf}}$ are surface heat and FW fluxes, respectively; F_H^{Stor} and $F_{\mathrm{FW}}^{\mathrm{Stor}}$ are heat and FW storage fluxes, respectively; V_{in} is the inflow volume transport associated with the water-mass transformation in the Arctic Ocean; Θ_{in} and S_{in} are transport-weighted inflow potential temperature and salinity, respectively; and $\Theta_{\mathrm{out}}^{oi}$ and S_{out}^{oi} are transport-weighted outflow potential temperature and salinity including the sea ice contribution, respectively. See T2018 for the derivations.

The overall mean seasonal cycles of inflow and outflow water properties from October 2004 to May 2010 are shown in Fig. 6. As indicated by T2018 with 1-yr data, Θ_{in} and S_{in} have around 3–5-months phase difference in their seasonal cycles. Whereas Θ_{in} has maxima in August–October and minima in April–May, S_{in} has maxima in January–March and minima in July–August. The average seasonality in Θ_{in} ranges between 2° and 5°C, and that in S_{in} ranges between 34.4 and 34.8. The seasonality of $\Theta_{\mathrm{out}}^{oi}$ and S_{out}^{oi} are mostly in phase as they form a nearly straight line on the θ–S plane. Although most of these features were identified in T2018, this study confirms these are the prominent signals in seasonality by using nearly 6 years of data.

We point out this temperature–salinity space diagram is a useful metric to diagnose the performance of different numerical ocean models and climate models. This single diagram presents the water-mass properties of the inflow and outflow, and the overall water-mass transformation that happens in the Arctic Ocean due to the surface heat flux and surface FW flux as summarized by Haine (2021). Mayer et al. (2019) already exploit our HT estimates to gain our understanding on the performance of reanalysis models (note that our HT and FWT estimates were published on Pangaea as a dataset in 2019; Tsubouchi et al. 2019). By comparing our HT estimate described in this study with that in various reanalysis models, Mayer et al. (2019) identify that reanalysis models tend to underestimate ocean heat transport to the Arctic Ocean by 10%–20% (i.e., surface heat loss from the ocean to the atmosphere in the models tend to be weak, indicating that models may be struggling to capture some processes correctly). Direct

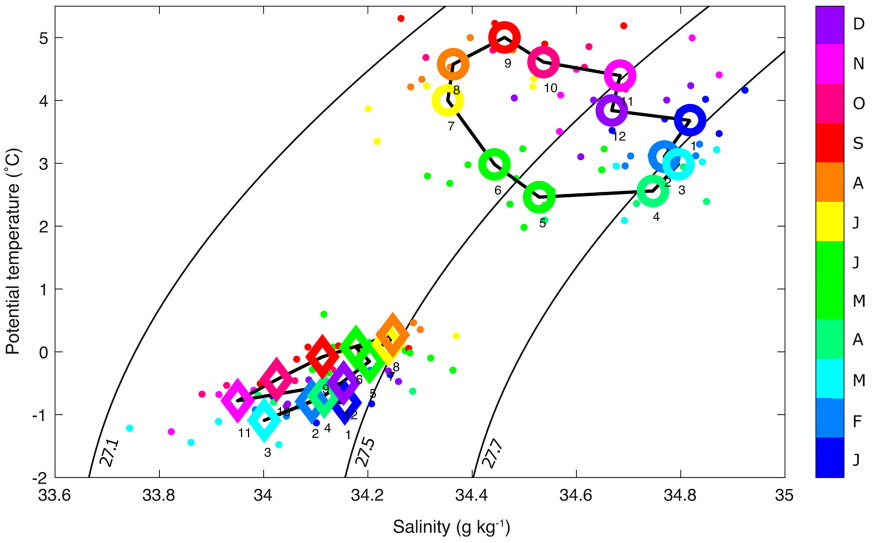

FIG. 6. Mean seasonal cycles of volume transport-weighted inflow properties of Θ_{in} and S_{in} (open circles) and outflow properties of Θ^{oi}_{out} and S^{oi}_{out} as open diamonds in the temperature–salinity space. The number at each symbol shows the number of months from January (month 1) to December (month 12). Individual 68-month estimates are shown as small dots. Color represents corresponding months both for the mean seasonal cycle and 68 individual months (small dots). Conventional water-mass density boundaries are shown in black. Corresponding potential densities are 27.1, 27.5, and 27.7 kg m^{-3} as in Rudels et al. (2008).

comparison of the estimated mean water-mass properties of the inflow and outflow (such as in, e.g., Fig. 6) with reanalysis models will shed light on where the differences may come from.

4. Discussion

a. *Fram Strait deep water*

We first discuss our estimate of the lower limb of the overturning circulation in the Arctic. Our estimate of 2.9 Sv is probably too large considering the overflow that crosses the Greenland–Scotland Ridge (Østerhus et al. 2019) and water-mass transformation that takes place in the Nordic seas by deep water formation in the Greenland Sea (Swift and Aagaard 1981) and densification of Atlantic Water in the Norwegian Sea (Mauritzen 1996). Based on over 20 years of historical observations, Østerhus et al. (2019) estimate that the total dense overflow across the Greenland–Scotland Ridge is 5.8 Sv. Exploiting Østerhus et al.'s (2019) historical observations with an inverse model, Tsubouchi et al. (2021) estimates that the Nordic seas can produce up to 4.0 Sv of overflow water and the Arctic Ocean including the Barents Sea may produce around 1.5 Sv of overflow water. This estimate of 1.5 compares to the estimate of 2.9 in this study. The large value obtained in the current study for the lower limb overturning cell in the Arctic is likely related to our large estimate of 1.4 Sv of southward flow in DW (below 1500 m), where we expect near-zero net volume transport. Based on historical hydrographic observations in the Greenland Sea and the Eurasian Basin of the Arctic Ocean, Somavilla et al. (2013) estimates the deep water exchange in Fram Strait as 0.4 Sv of northward flow of Eurasian Basin Deep Water to account for the warming and increasing in salinity in the Greenland Sea. The discrepancy with our estimate is most likely due to the sparse horizontal coverage of the moorings in Fram Strait and the vertical resolution of the velocity observations on the moorings that our estimate is based on (see, e.g., von Appen et al. 2015).

b. *Boundary transports, surface fluxes, and storage fluxes*

We discuss the meaning of the obtained boundary transports, in terms of their relation to the surface fluxes in absence of storage within the Arctic Ocean. Although this is already addressed in T2018, we discuss this topic to highlight its value and to address future improvements to the inverse model. Our inverse model does not account for the storage flux terms both in mass and salt. This means that horizontal salt transport across the gateway boundary is always balanced each month because there is no salt input by surface FW flux. At the same time, net export of seawater by the ocean plus sea ice volume transport [$\sim O(0.1$ Sv)] is balanced with the surface FW flux each month through mass conservation. This is achieved as the lower salinity outflow including sea ice (S^{oi}_{out}) from the Arctic Ocean carries the same amount of salt that is imported to the Arctic Ocean by the inflow with higher salinity (S_{in}). In this way, our surface FW flux is an "inferred" quantity derived from the pan-Arctic hydrographic sections. For the heat, surface heat flux is "inferred" by the temperature difference between inflow and outflow. These inferred surface fluxes are valuable because these quantities are poorly observed and poorly constrained by numerical models (Bacon

et al. 2022). These inferred surface heat and FW flux were already used to validate surface heat fluxes in reanalysis models (Mayer et al. 2019) and surface FW fluxes in reanalysis models (Winkelbauer et al. 2022) that helps to identify which reanalysis products represent the surface fluxes better in the Arctic Ocean.

We note our "inferred" surface FW flux of 156 ± 61 mSv likely has a negative bias of ~30 mSv as discussed in section 3c. In addition, our study period of 2004–10 is associated with a period of accumulation of FW content in the Beaufort gyre (Proshutinsky et al. 2019) and a period of reduced FW export through Davis Strait inferred from downstream hydrographic measurements on the Labrador Shelf over seven decades (Florindo-López et al. 2020). These conditions could explain the difference between our surface FW flux estimate and the state-of-art reanalysis and GRACE based estimate of atmospheric and terrestrial FW flux of 6560 $km^3\ yr^{-1}$ (equivalent to 208 mSv) over the period of 1993–2018 by Winkelbauer et al. (2022).

For future improvements of the Arctic boundary transports, we recommend to include Arctic Ocean storage estimates in obtaining the monthly solutions as well as to include the observed overflow water estimates across the Greenland–Scotland Ridge (Østerhus et al. 2019) as an additional constraint. As discussed by Bacon et al. (2022), measurements are available to estimate the storage fluxes of heat and FW. These are satellite measurements of GRACE and altimeter, and hydrographic measurements by ice-tethered profiler (ITP). Rabe et al. (2014) quantify the long-term change of FW content in the Arctic Ocean from 1992 to 2012, and of which an update to 2018 is currently on its way (M. Vredenborg et al. 2023, unpublished manuscript). In addition, Armitage et al. (2016) show the possibility to measure FW content change with remote sensing. Errors and uncertainties of these quantities need to be assessed to quantify the storage flux terms. For the inclusion of overflow estimates across the Greenland–Scotland Ridge as an additional constraint, additional unknowns for specific water masses may need to be considered so that adjustments on DW export will, for example, not directly affect the well observed AW inflow through Fram Strait. Errors on the additional overflow water constraints and uncertainties between vertically uniform adjustments and water-mass-specific adjustments need to be examined.

c. *Ambiguity of reference values*

It is widely recognized that the relative temperature transport and relative FW transport estimates through single gateways are heavily dependent on the choice of reference values (e.g., Dickson et al. 2007; Schauer and Beszczynska-Möller 2009; Tsubouchi et al. 2012; Bacon et al. 2015). Schauer and Losch (2019) urge to abandon the use of relative temperature transport and relative FW transport in single gateways completely in climate science. Yet, there are many studies that quantify the relative ocean temperature and relative FW transport estimates through single gateways and discuss their role related to ongoing Arctic climate changes. In this study, we have obtained the 68-month mean mass and salt balanced velocity field (Fig. 2), which we use to demonstrate the problems. Although this is already done by Tsubouchi et al. (2012) with summer 2005 hydrographic data, it is worthwhile to demonstrate this again with the nearly 6-yr mooring-based hydrographic sections that capture the main features of the ocean circulation through the Arctic boundary.

Figure 7a shows the cumulative relative temperature transport around the Arctic Ocean boundary with different reference temperatures. We demonstrate results using 1.01° ± 0.18°C (boundary mean potential temperature that changes from one month to another), 0.0°C, and seawater freezing temperature of −1.8°C. By integrating across the boundary all three lines end up with the same point of 151 TW that is the long-term mean ocean HT. In contrast, the integration results across part of the section differ significantly. Thus, integrated temperature transport does not change with the choice of the reference temperature, but temperature transport in each individual portion of the boundary, i.e., individual gateways, does change. For example, for the WSC in eastern Fram Strait, it changes from 33 TW-equivalent (TW-eq) with reference temperature of 1.01° ± 0.18°C to 113 TW-eq with reference temperature of −1.8°C.

Figure 7b shows the cumulative relative FWT around the boundary with different reference salinity, such as 34.70 ± 0.02 (boundary mean salinity that changes from one month to another), 34.8, and 35.0. The relative FWT has a similar caveat to that of relative ocean temperature transport. The integrated relative FWT around the boundary is hardly affected by the choice of the reference salinity and comes out as 102 mSv (the long-term mean ocean FWT), but the relative FWTs in each portion of the section (and hence each individual gateway) differ significantly. For the EGC in western Fram Strait, for instance, it changes from −4 ± 11 mSv-equivalent (mSv-eq) using reference salinity of 34.70 ± 0.02 to 56 ± 13 mSv-eq using reference salinity of 35.0. To be precise, the integrated relative FWT around the boundary is also affected by the choice of reference salinity. This is because the reference salinity appears in the denominator of the relative FWT equation. As discussed in Tsubouchi et al. (2012), a "sensible" choice of the reference salinity (between 34.8 and 35.2) only introduces an error of ~1% in the integrated relative FWT.

Here is our standpoint on the reference value issue: Scientists must be aware of the ambiguities and caveats of quantified relative ocean temperature transport and relative FW transport estimates in single gateways. We urge the use of different terms and units to distinguish between the two different quantities depending on their sensitivity to reference values, such as HT (W) versus relative temperature transport (W-eq) for heat and FWT (mSv) versus relative FWT (mSv-eq) for FW. This was already done by Talley (2003), Talley (2008), and T2018. The relative temperature transport and relative FWT in single gateways can be very different, both their mean values and temporal variabilities [Figs. 3 and 4 in Schauer and Losch (2019)]. We argue that it is not useful to interpret relative temperature and FW transports in single gateways in the context of their impact on heat and FW storage (or changes therein) in the Arctic Ocean.

5. Summary and conclusions

This study provides observation-based estimates of the overturning circulation in the Arctic Ocean and associated

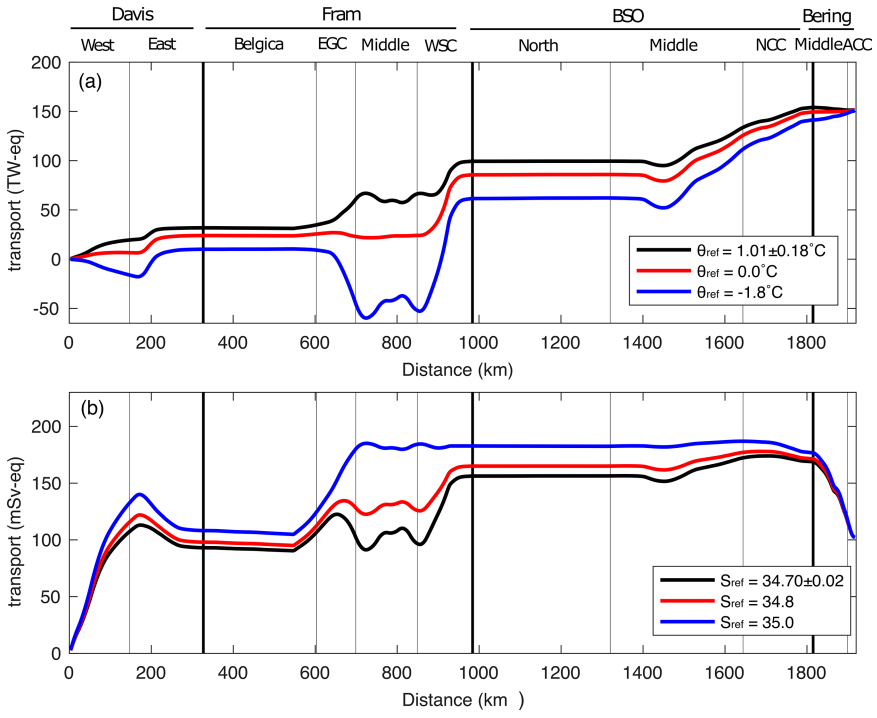

FIG. 7. (a) The 68-month mean cumulative relative temperature transport around the Arctic boundary (TW-eq) with different reference temperature: time-varying mean potential temperature across the section of 1.01° ± 0.18°C in black, 0.0°C in red, and −1.8°C in blue. (b) The 68-month mean cumulative relative FWT around the Arctic boundary (mSv-eq) with different reference salinity: time-varying mean salinity across the section of 34.70 ± 0.02 in black, 34.8 in red, and 35.0 in blue.

heat transport (HT) and freshwater transport (FWT) time series based on year-round hydrographic and current measurements during October 2004 to May 2010. A box inverse model is applied to obtain the pan-Arctic scale mass and salt balanced velocity fields over the period (Tsubouchi et al. 2019). The main results of this study are summarized as follows:

1) The overturning circulation in the Arctic Ocean is quantified for the first time from moored measurements: AW is transformed into two different water masses in the Arctic Ocean at a rate of 4.3 Sv. Combined with 0.7 Sv of Bering Strait inflow and 0.15 Sv of surface FW flux, 2.2 Sv flows back to the south through Davis Strait and western Fram Strait as the upper limb of the overturning circulation, while the remaining 2.9 Sv returns to the south through Fram Strait as the lower limb of the Arctic overturning.
2) We diagnose the existence of three overturning cells, of which the lower limb overturning shows the largest temporal fluctuations with maximum strength in winter. The latter is likely related to the seasonally wind-driven circulation.
3) The long-term mean HT is 180 ± 57 TW (mean ± standard deviation of monthly means) with a methodological uncertainty of 20 TW. It has a clear seasonality: the highest of ~260 TW in November and the lowest of ~110 TW in May.
4) The long-term mean FWT is 156 ± 91 mSv (mean ± standard deviation of monthly means) with a methodological uncertainty of 61 mSv and a potential offset of ~30 mSv. It has a substantial seasonality: the highest of ~260 mSv in March and the lowest of ~40 mSv in August.
5) We demonstrate the ambiguities and caveats to quantify the relative temperature transport and relative FW transport in single gateways. Proper understanding of the ambiguity will lead to sensible interpretations of the quantified estimates and the ocean's role on the changing Arctic climate system at large. We urge one to distinguish two different transport quantities through terminology and units.

Last, there are a few sustained basinwide scale mooring arrays in the North Atlantic to continuously monitor the temporal variability of the AMOC and associated HT and FWT (Frajka-Williams et al. 2019). Together with insights from these sustained observations, the overturning circulation in the Arctic Ocean and associated HT and FWT time series should be 1) extended over the entire past observational period up to present, 2) updated regularly in the future, and 3) considered to be improved with including storage terms in the Arctic Ocean. These will provide vital information to better understand the variability of the AMOC and allow us to identify trends or potential shifts that may happen in the future.

Acknowledgments. The Davis Strait mooring data were collected by the University of Washington, Seattle, Washington [principal investigator (PI) C. Lee], with funding from NSF Grant (ARC-1022472). The Bering Strait mooring data were

collected by University of Washington, Seattle, Washington, and the University of Alaska Fairbanks, Fairbanks, Alaska (PIs R. Woodgate and T. Weingartner), with funding from NSF Grant (NFS-0856786), and the NOAA-RUSALCA program. The BSO mooring data were collected by IMR, Bergen, Norway (PI R. Ingvaldsen). The Fram Strait mooring data from 2004 to 2010 were collected by AWI, Bremerhaven, Germany (PI U. Schauer), and NPI, Tromsø, Norway (PI E. Hansen). "DOBOX 4.2" (Morgan 1995) is used for the box inverse model. Support for this study came from the Alfred Wegener Institute, Helmholtz Centre for Polar and Marine Research, and from the Helmholtz Infrastructure Initiative FRAM. Author T. Tsubouchi was funded by the EU Horizon 2020 Marie Skłodowska-Curie Grant ARCGATE (652757).

Data availability statement. The Davis Strait mooring data and objectively mapped sections (https://iop.apl.washington.edu/downloads.php), Bering Strait mooring data (http://psc.apl.washington.edu/BeringStrait.html), central and eastern Fram Strait mooring data (https://doi.pangaea.de/10.1594/PANGAEA.150006), and western Fram Strait mooring data (https://doi.org/10.21334/npolar.2019.8bb85388) are all available online. The BSO mooring data are available on request. The CTD data in BSO are available at the ICES database (https://www.ices.dk/data/Pages/default.aspx). The PIOMAS sea ice data (http://psc.apl.uw.edu/research/projects/arctic-sea-ice-volume-anomaly/data/) and the volume, heat, and FW transport time series presented in this paper (https://doi.pangaea.de/10.1594/PANGAEA.909966) are available online.

REFERENCES

Armitage, T. W. K., S. Bacon, A. L. Ridout, S. F. Thomas, Y. Aksenov, and D. J. Wingham, 2016: Arctic sea surface height variability and change from satellite radar altimetry and GRACE, 2003–2014. *J. Geophys. Res. Oceans*, **121**, 4303–4322, https://doi.org/10.1002/2015JC011579.

Bacon, S., Y. Aksenov, S. Fawcett, and G. Madec, 2015: Arctic mass, freshwater and heat fluxes: Methods and modelled seasonal variability. *Philos. Trans. Roy. Soc.*, **A373**, 20140169, https://doi.org/10.1098/rsta.2014.0169.

——, A. C. Naveira Garabato, Y. Aksenov, N. J. Brown, and T. Tsubouchi, 2022: Arctic Ocean boundary exchanges: A review. *Oceanography*, **35**, 94–102, https://doi.org/10.5670/oceanog.2022.133.

Beszczynska-Möller, A., E. Fahrbach, U. Schauer, and E. Hansen, 2012: Variability in Atlantic water temperature and transport at the entrance to the Arctic Ocean, 1997–2010. *ICES J. Mar. Sci.*, **69**, 852–863, https://doi.org/10.1093/icesjms/fss056.

——, W.-J. von Appen, and E. Fahrbach, 2015: Physical oceanography and current meter data from moorings in the Fram Strait, 1997–2012. PANGAEA, accessed 12 July 2023, https://doi.org/10.1594/PANGAEA.150006.

Burgard, C., and D. Notz, 2017: Drivers of Arctic Ocean warming in CMIP5 models. *Geophys. Res. Lett.*, **44**, 4263–4271, https://doi.org/10.1002/2016GL072342.

Cunningham, S. A., and Coauthors, 2007: Temporal variability of the Atlantic meridional overturning circulation at 26.5°N. *Science*, **317**, 935–938, https://doi.org/10.1126/science.1141304.

Curry, B., C. M. Lee, B. Petrie, R. E. Moritz, and R. Kwok, 2014: Multiyear volume, liquid freshwater, and sea ice transports through Davis Strait, 2004–10. *J. Phys. Oceanogr.*, **44**, 1244–1266, https://doi.org/10.1175/JPO-D-13-0177.1.

de Steur, L., 2019: Moored current meter data from the western Fram Strait 1997–2009. Norwegian Polar Institute, accessed 12 July 2023, https://doi.org/10.21334/npolar.2019.8bb85388.

——, E. Hansen, C. Mauritzen, A. Beszczynska-Möller, and E. Fahrbach, 2014: Impact of recirculation on the East Greenland Current in Fram Strait: Results from moored current meter measurements between 1997 and 2009. *Deep-Sea Res. I*, **92**, 26–40, https://doi.org/10.1016/j.dsr.2014.05.018.

Dickson, R., B. Rudels, S. Dye, M. Karcher, J. Meincke, and I. Yashayaev, 2007: Current estimates of freshwater flux through Arctic and subarctic seas. *Prog. Oceanogr.*, **73**, 210–230, https://doi.org/10.1016/j.pocean.2006.12.003.

——, J. Meincke, and P. Rhines, 2008: *Arctic-Subarctic Ocean Fluxes: Defining the Role of the Northern Seas in Climate*. Springer, 736 pp.

Druckenmiller, M. L., R. L. Thoman, and T. A. Moon, Eds., 2022: Arctic Report Card 2022: Executive summary. NOAA Tech. Rep. OAR ARC 22-01, 4 pp., https://doi.org/10.25923/yjx6-r184.

Florindo-López, C., and Coauthors, 2020: Arctic Ocean and Hudson Bay freshwater exports: New estimates from seven decades of hydrographic surveys on the Labrador shelf. *J. Climate*, **33**, 8849–8868, https://doi.org/10.1175/JCLI-D-19-0083.1.

Frajka-Williams, E., and Coauthors, 2019: Atlantic meridional overturning circulation: Observed transport and variability. *Front. Mar. Sci.*, **6**, 260, https://doi.org/10.3389/fmars.2019.00260.

Ganachaud, A., and C. Wunsch, 2000: Improved estimates of global ocean circulation, heat transport and mixing from hydrographic data. *Nature*, **408**, 453–457, https://doi.org/10.1038/35044048.

——, and ——, 2003: Large-scale ocean heat and freshwater transports during the World Ocean Circulation Experiment. *J. Climate*, **16**, 696–705, https://doi.org/10.1175/1520-0442(2003)016<0696:LSOHAF>2.0.CO;2.

Haine, T. W. N., 2021: A conceptual model of polar overturning circulations. *J. Phys. Oceanogr.*, **51**, 727–744, https://doi.org/10.1175/JPO-D-20-0139.1.

Hall, M. M., and H. L. Bryden, 1982: Direct estimates and mechanisms of ocean heat-transport. *Deep-Sea Res.*, **29A**, 339–359, https://doi.org/10.1016/0198-0149(82)90099-1.

Hansen, B., and S. Østerhus, 2000: North Atlantic–Nordic seas exchanges. *Prog. Oceanogr.*, **45**, 109–208, https://doi.org/10.1016/S0079-6611(99)00052-X.

Ilıcak, M., and Coauthors, 2016: An assessment of the Arctic Ocean in a suite of interannual CORE-II simulations. Part III: Hydrography and fluxes. *Ocean Model.*, **100**, 141–161, https://doi.org/10.1016/j.ocemod.2016.02.004.

Ingvaldsen, R. B., L. Asplin, and H. Loeng, 2004: The seasonal cycle in the Atlantic transport to the Barents Sea during the years 1997–2001. *Cont. Shelf Res.*, **24**, 1015–1032, https://doi.org/10.1016/j.csr.2004.02.011.

IPCC, 2021: *Climate Change 2021: The Physical Science Basis*. Cambridge University Press, 2391 pp., https://doi.org/10.1017/9781009157896.

Johnson, M., and Coauthors, 2012: Evaluation of Arctic sea ice thickness simulated by Arctic Ocean model intercomparison project models. *J. Geophys. Res.*, **117**, C00D13, https://doi.org/10.1029/2011JC007257.

Karpouzoglou, T., L. de Steur, and P. A. Dodd, 2023: Freshwater transport over the northeast Greenland shelf in Fram Strait. *Geophys. Res. Lett.*, **50**, e2022GL101775, https://doi.org/10.1029/2022GL101775.

Kovacs, A., 1996: Sea Ice. Part 1. Bulk salinity versus ice floe thickness. CRREL Rep. 96-7, 23 pp., https://apps.dtic.mil/sti/pdfs/ADA312027.pdf.

Le Bras, I., F. Straneo, M. Muilwijk, L. H. Smedsrud, F. Li, M. S. Lozier, and N. P. Holliday, 2021: How much Arctic fresh water participates in the subpolar overturning circulation? *J. Phys. Oceanogr.*, **51**, 955–973, https://doi.org/10.1175/JPO-D-20-0240.1.

Lozier, M. S., and Coauthors, 2019: A sea change in our view of overturning in the subpolar North Atlantic. *Science*, **363**, 516–521, https://doi.org/10.1126/science.aau6592.

Mauritzen, C., 1996: Production of dense overflow waters feeding the North Atlantic across the Greenland-Scotland Ridge. Part 2. An inverse model. *Deep-Sea Res. I*, **43**, 807–809, https://doi.org/10.1016/0967-0637(96)00038-6.

Mayer, M., S. Tietsche, L. Haimberger, T. Tsubouchi, J. Mayer, and H. Zuo, 2019: An improved estimate of the coupled Arctic energy budget. *J. Climate*, **32**, 7915–7934, https://doi.org/10.1175/JCLI-D-19-0233.1.

Morgan, P. P., 1995: Box inverse modelling with DOBOX 4.2. CSIRO Marine Laboratories Rep. 225, 32 pp., http://www.cmar.csiro.au/e-print/open/CMReport_225.pdf.

Østerhus, S., and Coauthors, 2019: Arctic Mediterranean exchanges: A consistent volume budget and trends in transports from two decades of observations. *Ocean Sci.*, **15**, 379–399, https://doi.org/10.5194/os-15-379-2019.

Polyakov, I. V., and Coauthors, 2017: Greater role for Atlantic inflows on sea-ice loss in the Eurasian Basin of the Arctic Ocean. *Science*, **356**, 285–291, https://doi.org/10.1126/science.aai8204.

Proshutinsky, A., and Coauthors, 2019: Analysis of the Beaufort Gyre freshwater content in 2003–2018. *J. Geophys. Res. Oceans*, **124**, 9658–9689, https://doi.org/10.1029/2019JC015281.

Rabe, B., and Coauthors, 2014: Arctic Ocean basin liquid freshwater storage trend 1992–2012. *Geophys. Res. Lett.*, **41**, 961–968, https://doi.org/10.1002/2013GL058121.

Rudels, B., M. Marnela, and P. Eriksson, 2008: Constraints on estimating mass, heat and freshwater transports in the Arctic Ocean: An exercise. *Arctic-Subarctic Ocean Fluxes: Defining the Role of the Northern Seas in Climate*, R. R. Dickson, J. Meincke, and P. Rhines, Eds., Springer, 315–341.

Schauer, U., and A. Beszczynska-Möller, 2009: Problems with estimation and interpretation of oceanic heat transport – Conceptual remarks for the case of Fram Strait in the Arctic Ocean. *Ocean Sci.*, **5**, 487–494, https://doi.org/10.5194/os-5-487-2009.

——, and M. Losch, 2019: "Freshwater" in the ocean is not a useful parameter in climate research. *J. Phys. Oceanogr.*, **49**, 2309–2321, https://doi.org/10.1175/JPO-D-19-0102.1.

Somavilla, R., U. Schauer, and G. Budéus, 2013: Increasing amount of Arctic Ocean deep waters in the Greenland Sea. *Geophys. Res. Lett.*, **40**, 4361–4366, https://doi.org/10.1002/grl.50775.

Swift, J. H., and K. Aagaard, 1981: Seasonal transitions and water mass formation in the Iceland and Greenland seas. *Deep-Sea Res.*, **28A**, 1107–1129, https://doi.org/10.1016/0198-0149(81)90050-9.

Talley, L. D., 2003: Shallow, intermediate, and deep overturning components of the global heat budget. *J. Phys. Oceanogr.*, **33**, 530–560, https://doi.org/10.1175/1520-0485(2003)033<0530:SIADOC>2.0.CO;2.

——, 2008: Freshwater transport estimates and the global overturning circulation: Shallow, deep and throughflow components. *Prog. Oceanogr.*, **78**, 257–303, https://doi.org/10.1016/j.pocean.2008.05.001.

The IMBIE Team, 2020: Mass balance of the Greenland Ice Sheet from 1992 to 2018. *Nature*, **579**, 233–239, https://doi.org/10.1038/s41586-019-1855-2.

Tsubouchi, T., and Coauthors, 2012: The Arctic Ocean in summer: A quasi-synoptic inverse estimate of boundary fluxes and water mass transformation. *J. Geophys. Res.*, **117**, C01024, https://doi.org/10.1029/2011JC007174.

——, and Coauthors, 2018: The Arctic Ocean seasonal cycles of heat and freshwater fluxes: Observation-based inverse estimates. *J. Phys. Oceanogr.*, **48**, 2029–2055, https://doi.org/10.1175/JPO-D-17-0239.1.

——, and Coauthors, 2019: The Arctic Ocean volume, heat and fresh water transports time series from October 2004 to May 2010. PANGAEA, accessed 12 July 2023, https://doi.org/10.1594/PANGAEA.909966.

——, K. Våge, B. Hansen, K. M. H. Larsen, S. Østerhus, C. Johnson, S. Jónsson, and H. Valdimarsson, 2021: Increased ocean heat transport into the Nordic seas and Arctic Ocean over the period 1993–2016. *Nat. Climate Change*, **11**, 21–26, https://doi.org/10.1038/s41558-020-00941-3.

Uotila, P., and Coauthors, 2018: An assessment of ten ocean reanalyses in the polar regions. *Climate Dyn.*, **52**, 1613–1650, https://doi.org/10.1007/s00382-018-4242-z.

Våge, K., R. S. Pickart, M. A. Spall, H. Valdimarsson, S. Jónsson, D. J. Torres, S. Østerhus, and T. Eldevik, 2011: Significant role of the North Icelandic jet in the formation of Denmark Strait overflow water. *Nat. Geosci.*, **4**, 723–727, https://doi.org/10.1038/ngeo1234.

von Appen, W. J., U. Schauer, R. Somavilla, E. Bauerfeind, and A. Beszczynska-Möller, 2015: Exchange of warming deep waters across Fram Strait. *Deep-Sea Res. I*, **103**, 86–100, https://doi.org/10.1016/j.dsr.2015.06.003.

——, ——, T. Hattermann, and A. Beszczynska-Möller, 2016: Seasonal cycle of mesoscale instability of the West Spitsbergen Current. *J. Phys. Oceanogr.*, **46**, 1231–1254, https://doi.org/10.1175/JPO-D-15-0184.1.

von Schuckmann, K., and Coauthors, 2020: Heat stored in the Earth system: Where does the energy go? *Earth Syst. Sci. Data*, **12**, 2013–2041, https://doi.org/10.5194/essd-12-2013-2020.

Wang, Q., and Coauthors, 2016: An assessment of the Arctic Ocean in a suite of interannual CORE-II simulations. Part II: Liquid freshwater. *Ocean Model.*, **99**, 86–109, https://doi.org/10.1016/j.ocemod.2015.12.009.

Winkelbauer, S., M. Mayer, V. Seitner, E. Zsoter, H. Zuo, and L. Haimberger, 2022: Diagnostic evaluation of river discharge into the Arctic Ocean and its impact on oceanic volume transports. *Hydrol. Earth Syst. Sci.*, **26**, 279–304, https://doi.org/10.5194/hess-26-279-2022.

Woodgate, R. A., 2018: Increases in the Pacific inflow to the Arctic from 1990 to 2015, and insights into seasonal trends and driving mechanisms from year-round Bering Strait mooring data. *Prog. Oceanogr.*, **160**, 124–154, https://doi.org/10.1016/j.pocean.2017.12.007.

Wunsch, C., 1996: *The Ocean Circulation Inverse Problem*. Cambridge University Press, 442 pp.

Zhang, J., and D. A. Rothrock, 2003: Modeling global sea ice with a thickness and enthalpy distribution model in generalized curvilinear coordinates. *Mon. Wea. Rev.*, **131**, 845–861, https://doi.org/10.1175/1520-0493(2003)131<0845:MGSIWA>2.0.CO;2.